

# Measurement of Oceanic Wind Vector Using Satellite Microwave Radiometers

Frank J. Wentz

**Abstract**—We investigate the possibility of retrieving both wind speed and direction from microwave radiometer measurements of the ocean. The data for this investigation are the Special Sensor Microwave/Imager (SSM/I) measurements collocated with buoy reports from the National Data Buoy Center (NDBC). A physically based algorithm is used to retrieve the wind speed. The rms difference between the SSM/I and buoy wind speed is 1.6 m/s for 3321 comparisons. We find that the SSM/I minus buoy wind speed difference is correlated with wind direction. This correlation is due to a wind direction signal in the brightness temperatures ( $T_B$ ). For moderate wind speeds, the v-pol upwind  $T_B$  is about 2 K higher than the downwind  $T_B$ . For h-pol observations, the  $T_B$  maximum occurs at crosswind rather than upwind and is approximately 3.5 K higher than the minimum at downwind. When this wind direction signal is removed, the rms difference between the SSM/I and buoy winds reduces to 1.3 m/s. The wind direction signal is used to make global, low-resolution maps of the monthly mean oceanic wind vector. Finally, we assess the wind direction sensing capability of a prospective two-look satellite radiometer. Preliminary computer simulations indicate a direction accuracy of  $15^\circ$ .

**Keywords**—Microwave radiometers, ocean wind vector, SSM/I.

## I. INTRODUCTION

It is well known that the microwave emission from the ocean depends on surface roughness. A calm sea surface is characterized by a highly polarized emission. When the surface becomes rough, the emission increases and becomes less polarized (except at incidence angles above  $60^\circ$  for which the vertically polarized emission decreases). There are three mechanisms that are responsible for this variation in the emissivity. First, surface waves having wavelengths long compared to the radiation wavelength mix the horizontal and vertical polarization states and change the local incidence angle. This phenomenon can be modeled as a collection of tilted facets, each acting as an independent specular surface [19]. The second mechanism is sea foam. This mixture of air and water increases in the emissivity for both polarizations. Sea foam models have been developed by Stogryn [21] and Smith [18]. The third roughness effect is the diffraction of microwaves by surface waves that are small compared to the radiation wavelength. Rice [17] provided the basic formulation for computing scattering from a slightly rough surface. Wu and Fung [28] and Wentz [22] applied this scattering formulation to

the problem of computing the emissivity of a wind-roughened sea surface.

These three effects can be parameterized in terms of the rms slope of the large-scale roughness, the fractional foam coverage, and the rms height of the small-scale waves. Each of these parameters depends on wind speed. Cox and Munk [4], Monahan and O'Muircheartaigh [15], and Mitsuyasu and Honda [14] derived wind speed relationships for the three parameters, respectively. These wind speed relationships in conjunction with the tilt+foam+diffraction model provide the means to compute the sea-surface emissivity. Computations of this type have been done by Wentz [22], [23] and are in general agreement with microwave observations.

In addition to depending on wind speed, the large-scale rms slope and the small-scale rms height depend on wind direction. The probability density function of the sea-surface slope is skewed in the alongwind axis and has a larger alongwind variance than crosswind variance [4]. The rms height of capillary waves is very anisotropic [14]. The capillary waves traveling in the alongwind direction have a greater amplitude than those traveling in the crosswind direction. Another type of directional dependence occurs because the foam and capillary waves are not uniformly distributed over the underlying structure of large-scale waves. Smith's [18] aircraft radiometer measurements show that the forward plunging side of a breaking wave exhibits distinctly warmer microwave emissions than does the back side. In addition, the capillary waves tend to cluster on the downwind side of the larger gravity waves [3], [10]. The dependence of foam and capillary waves on the underlying structure produces an upwind-downwind asymmetry in the sea-surface emissivity.

The anisotropy of capillary waves is responsible for the observed dependence of radar backscattering on wind direction [8]. The upwind radar return is considerably higher than the crosswind return. Also, the modulation of the capillary waves by the underlying gravity waves causes the upwind return to be generally higher than the downwind return. These directional characteristics of the radar return have provided the means to sense wind direction from aircraft and satellite scatterometers [9].

There has been little research into the possibility of obtaining wind direction from passive microwave sensors. One reason for this is that the tilt+foam model predicts that the directional effect is only a few degrees Kelvin. Until recently, calibration problems made it difficult for aircraft and satellite radiometers to detect this small directional signal. Kravtsov *et al.* [12] did point out that for nadir observations the diffraction

Manuscript received September 10, 1991. This research was supported by the National Aeronautics and Space Administration under contracts NAS8-38075 with Marshall Space Flight Center and NAS5-30929 with Goddard Space Flight Center.

The author is with Remote Sensing Systems, Santa Rosa, CA 95404.  
IEEE Log Number 9202078.

model predicts a polarization anisotropy of several degrees Kelvin. This prediction seems to be confirmed by the nadir aircraft observations reported by Bespalova *et al.* [2]. When the polarization vector was in the alongwind wind direction, the aircraft measurements were 5 K higher than when the polarization vector was in the crosswind direction.

The recent advent of precision satellite microwave radiometers and the results of [2] prompted us to investigate the possibility of obtaining wind direction from conically scanning microwave radiometers, such as the Special Sensor Microwave Imager (SSM/I).

## II. SSM/I DATA SET

SSM/I is a microwave radiometer system flown on the Defense Meteorological Satellite Program (DMSP) satellites. Currently, there are two SSM/I's in operation, one on the DMSP F-8 satellite launched in June 1987 and the other on the F-10 satellite launched in December 1990. We will be using the data obtained from the F-8 satellite. This satellite is in a near-circular, sun-synchronous, and near-polar orbit, with an average altitude of 860 km and an inclination of 98.8°. The orbital period is 102 min, and the local time for the ascending equatorial crossing is 6:12 am. This orbit provides complete coverage of the Earth, except for two small circular sectors of 2.4° centered on the North and South poles.

SSM/I consists of seven separate total-power radiometers, each simultaneously measuring the microwave emission coming from the Earth and the intervening atmosphere. Dual-polarization measurements are taken at 19.35, 37.0, and 85.5 GHz, and only vertical polarization is observed at 22.235 GHz. The antenna system consists of a 61 by 66-cm offset parabolic reflector, which focuses the Earth radiation into a corrugated, broad-band, 7-port feedhorn. The parabolic reflector, feedhorn, and receivers spin as a unit about the nadir axis. The rotation period is 1.9 s. A cold sky reflector and a warm reference load are attached to the spin axis and do not rotate. The rotating feedhorn observes the fixed cold reflector and warm load once each scan. In this way, calibration observations are taken every scan.

The SSM/I antenna boresight is 45° off nadir and conically scans the Earth's surface along a circle that has a 900-km radius. Earth observations are taken on a 102.4° arc centered on the spacecraft subtrack in the aft direction. This arc corresponds to 1400-km wide swath. During each scan, the 85-GHz channels are sampled 128 times over the 102.4° arc. Observations at the lower three frequencies are taken only every other scan and are sampled 64 times over the arc. This sampling pattern results in a 12.5-km pixel spacing at 85 GHz and a 25-km pixel spacing at the lower frequencies. The 3-dB spatial resolutions of the 19, 22, 37, and 85-GHz channels are approximately 56, 45, 33, and 14 km, respectively. The sensor hardware is further described in [6]. The data coming from SSM/I consist of the following items:

1. Time of beginning of scan
2. Radiometer counts when viewing Earth reflector,  $C$
3. Radiometer counts when viewing warm load,  $C_w$
4. Radiometer counts when viewing cold reflector,  $C_c$

5. Physical temperature of warm load,  $T_w$
6. Various diagnostic parameters

The SSM/I orbit geometry is a known function of time, and hence the latitude and longitude of a given pixel can be computed from the time and the scan position. The incidence angle  $\theta_i$  and azimuth angle  $\phi$  for an observation can also be computed from the orbit geometry and scan position. The incidence angle  $\theta_i$  is defined as the angle made by the vector  $\mathbf{k}$  pointing from the pixel to the satellite and the vector  $\mathbf{n}$  that is normal to the Earth's geoid at the pixel location. The incidence angle for SSM/I is  $53^\circ \pm 0.2^\circ$ . The  $0.2^\circ$  variation is due to the eccentricity of the SSM/I orbit and the Earth's oblateness. The azimuth angle  $\phi$  is the angle between two vector, both of which are orthogonal to  $\mathbf{n}$ . The first vector is in the plane of incidence defined by  $\mathbf{n}$  and  $\mathbf{k}$ , and the second vector points toward North. The angle is defined such that  $\phi = 0^\circ$  corresponds to SSM/I looking North and  $\phi = 90^\circ$  corresponds to SSM/I looking East.

The intensity of the radiation entering the feedhorn is expressed in terms of an antenna temperature  $T_A$  in units of Kelvin degrees. Wentz [25] describes how the antenna temperature is computed from  $C$ ,  $C_w$ ,  $C_c$ , and  $T_w$ . The computation is essentially

$$T_A = [C(T_w - T_{Bc}) + (T_{Bc}C_h - T_wC_c)] / (C_h - C_c) \quad (1)$$

where  $T_{Bc}$  is the brightness temperature of cold space and varies from 2.7 K at 19 GHz to 3.2 K at 85 GHz. Two corrections are applied to  $T_A$ . The first is a correction to remove an error that occurs near one edge of the scan, where the  $T_A$ 's show a systematic 1 K drop-off. This effect was detected by stratifying the SSM/I data according to scan position and then averaging over one year. One explanation for this effect is that the feedhorn partially sees the cold reflector near the scan edge.

The second correction is a single offset that is applied to each channel. These offsets compensate for absolute errors in the measurements and in the geophysical model described in Section IV. For the 19V, 19H, 22V, 37V, and 37H channels, these offsets are 2.0, 3.5, 1.3, -1.6, and -0.2 K, respectively. The offsets are subtracted from the  $T_A$  value given by (1). The 22V, 37V, and 37H offsets are derived by requiring that the retrieved geophysical parameters have zero bias. The retrieval algorithm discussed below uses the 22V, 37V, and 37H channels to compute wind speed  $W$ , atmospheric columnar water vapor  $V$ , and liquid water absorption  $A_L$ . The wind speeds are compared to buoy winds, and the vapor contents are compared to radiosonde observations. In addition a histogram of the retrieved liquid water absorption is compared to a theoretical  $A_L$  histogram. The theoretical histogram is constructed by assuming an exponential decay probability density function for the true  $A_L$  and then adding Gaussian noise to simulate measurement error. The following three requirements are made.

1. The mean difference between the buoy and SSM/I wind speed is zero.
2. The mean difference between the radiosonde and SSM/I water vapor is zero.
3. The histogram of the SSM/I  $A_L$  is aligned with the theoretical histogram.

Condition 3 is essentially prohibiting large negative  $A_L$  values while requiring an abundance of  $A_L$  values near 0 corresponding to clear sky conditions. These three requirements are sufficient to determine the 22V, 37V, and 37H offsets. The 19V and 19H offsets are found by requiring a zero mean difference between the  $T_A$  observations and the geophysical model at 19 GHz. To compute the 19-GHz model values, the retrieved  $W$ ,  $V$ , and  $A_L$  values are used.

For geophysical interpretation of the received signal, the desired quantity is the intensity of radiation coming from the pixel being observed by the antenna boresight. This radiation intensity is expressed in terms of a brightness temperature  $T_B$  in units of Kelvin degrees. Although the antenna reception pattern is highly peaked in the boresight direction, some radiation is received from other directions. The reception from cold space, which comprises about 75% of the spherical area surrounding the antenna, has an appreciable effect on  $T_A$ . Also, there is some leakage of the orthogonal polarization through the feedhorn ports. To obtain the brightness temperature of a pixel, it is necessary to correct for the cold-space  $T_A$  contribution and the cross-polarization leakage. This correction takes the form

$$T_{Bv} = G_{vv}T_{Av} + G_{hv}T_{Ah} + G_{ov} \quad (2a)$$

$$T_{Bh} = G_{hh}T_{Ah} + G_{vh}T_{Av} + G_{oh} \quad (2b)$$

where  $T_{Av}$  and  $T_{Ah}$  are the v-pol and h-pol antenna temperature with the scan-edge and offset corrections applied.  $T_{Bv}$  and  $T_{Bh}$  are the v-pol and h-pol brightness temperatures of the pixel. Values for the  $G$  coefficients are given in [25]. The brightness temperatures of adjacent pixels also contribute to the  $T_A$  observation. This sidelobe problem is most serious in regions having large  $T_B$  gradients, such as coastlines, ice edges, and ocean storms. We do not correct for sidelobe effects.

### III. NDBC DATA SET

The National Data Buoy Center (NDBC) operates a network of moored buoys. For this investigation we obtain data from 19 NDBC buoys located in the Northeast Pacific, Northwest Atlantic, and Gulf of Mexico. This data set was prepared by Goodberlet *et al.* [5]. We use only buoys that are at least 100 km from land in order to avoid the problem of the SSM/I antenna sidelobes receiving land emission. Data are collected for the period from July 1987 through March 1988. The buoys measure a number of parameters including wind speed  $W$ , wind direction  $\phi_w$ , sea temperature  $T_s$ , and air temperature  $T_a$ . The buoys have two anemometer heights, 5 m and 10 m. To obtain a common reference height of 10 m, the wind speeds from the 5-m anemometers are increased by 6%.

For each buoy, a set of SSM/I overpass times are found. An SSM/I overpass is defined as those cases in which some portion of the SSM/I swath is within 50 km of the buoy location. For each SSM/I channel, the brightness temperatures within a 50-km radius of the buoy location are first averaged. In addition, the incidence angle  $\theta_i$  and azimuth angle  $\phi$  for the averaged  $T_B$  observation are found. The buoy reports are then

searched to find the two reports that bracket the overpass time. The buoy data from these two reports are interpolated to the overpass time. In most cases a buoy report is within 0.5 h of the overpass time. If there is no buoy report within 1.5 h of the overpass time, then no SSM/I versus buoy comparison is done. This procedure results in 3831 sets, with each set containing the averaged  $T_B$  for each of the seven channels,  $\theta_i$ ,  $\phi$ , and the following time-interpolated buoy data:  $W$ ,  $\phi_w$ ,  $T_s$  and  $T_a$ .

### IV. SSM/I WIND SPEED ALGORITHM

The algorithm for computing wind speed uses only the SSM/I 37-GHz channels. The procedure involves solving the following two equations in two unknowns.

$$T_{Bv} = F_v(W, \tau) \quad (3a)$$

$$T_{Bh} = F_h(W, \tau) \quad (3b)$$

where  $T_{Bv}$  and  $T_{Bh}$  are the 37-GHz vertically and horizontally polarized brightness temperature observations, respectively. The unknowns are wind speed  $W$  (m/s) and the total one-way atmospheric transmittance  $\tau$  along the viewing path of the radiometer. We will first derive the model functions  $F_v(W, \tau)$  and  $F_h(W, \tau)$  and then discuss how the two simultaneous equations are solved. In this model the wind speed is referenced to an anemometer height of 19.5 m. The upwelling brightness temperature seen by a satellite radiometer is given by the following expression [23].

$$F(W, \tau) = T_{Bu} + \tau[ET_s + (1 - E)(1 + \omega W)(T_{Bd} + \tau T_{Bc})]. \quad (4)$$

The subscript denoting polarization is now implicit. The quantities  $T_{Bu}$  and  $T_{Bd}$  are the upwelling and downwelling brightness temperatures due solely to the atmospheric emission and absorption. The quantity  $T_{Bc}$  is the brightness temperature of cold space and equals 2.8 K at 37 GHz. The emissivity of the sea surface is denoted by  $E$ . The sea-surface temperature is denoted by  $T_s$  and is in units of Kelvin degrees. The term  $(1 + \omega W)$  accounts for a small increase in the reflected atmospheric radiation due to surface scattering (as opposed to simple reflection). The coefficient  $\omega$  is given in Table I.

We assume that there is no significant scattering of radiation by the atmosphere. At 37 GHz, scattering occurs only when there is appreciable rain or ice in the field of view. The upward and downward atmospheric brightness temperatures for a nonscattering atmosphere are given by

$$T_{Bu} = (1 - \tau)T_u \quad (5a)$$

$$T_{Bd} = (1 - \tau)T_d \quad (5b)$$

where  $T_u$  and  $T_d$  are the effective air temperatures. If the air temperature  $T_a$  were constant (i.e., a zero lapse rate), then  $T_u$  and  $T_d$  would exactly equal  $T_a$ . In reality the air temperature in the troposphere usually decreases with altitude, and  $T_u$  and  $T_d$  are weighted averages of the air temperature, where the weight is approximately equal to the absorption along the propagation path.

TABLE I  
COEFFICIENTS FOR BRIGHTNESS TEMPERATURE MODEL AT SSM/I CHANNELS

Coeff.	Units	19V	19H	22V	37V	37H
$s_0$	K	1.6253E+2	0.8220E+2	1.6699E+2	1.8631E+2	0.9974E+2
$s_1$	none	-2.570E-1	-2.805E-1	-3.408E-1	-5.637E-1	-6.171E-1
$s_2$	K <sup>-1</sup>	1.729E-2	1.237E-2	1.735E-2	1.481E-2	1.437E-2
$s_3$	K <sup>-2</sup>	-1.177E-4	-0.925E-4	-1.036E-4	-0.296E-4	-0.707E-4
$s_4$	K deg <sup>-1</sup>	2.162E+0	-1.472E+0	2.164E+0	2.123E+0	-1.701E+0
$s_5$	deg <sup>-1</sup>	0.70E-2	0.21E-2	0.75E-2	1.17E-2	0.55E-2
$s_6$	K deg <sup>-2</sup>	4.5E-2	-1.6E-2	4.5E-2	4.1E-2	-1.9E-2
$s_7$	K <sup>-1</sup> deg <sup>-1</sup>	0.14E-4	-1.10E-4	0.02E-4	-0.71E-4	-1.27E-4
$\omega$	s m <sup>-1</sup>	4.89E-3	9.68E-3	3.78E-3	3.52E-3	8.55E-3
$m_1$	s m <sup>-1</sup>	0.623E-3	2.340E-3	0.634E-3	0.700E-3	4.100E-3
$m_2$	s m <sup>-1</sup>	3.462E-3	6.146E-3	3.305E-3	2.500E-3	7.300E-3
$\beta$	s m <sup>-1</sup> deg <sup>-1</sup>	-0.812E-4	0.806E-4	-0.868E-4	-1.193E-4	1.052E-4

To determine the effective air temperature, we use the 609 radiosonde reports described in [23]. The radiosonde profiles in conjunction with the oxygen and water vapor absorption coefficients given by Liebe [13] provide the means to compute  $\tau$ ,  $T_{Bu}$ , and  $T_{Bd}$ . A least-squares fit of (5) to the 609 sets of  $\tau$ ,  $T_{Bu}$  and  $T_{Bd}$  gives the following effective air temperatures for 37 GHz:

$$T_u = T_a - 14.6 \quad (6a)$$

$$T_d = T_a - 13.0 \quad (6b)$$

where  $T_a$  is the surface air temperature and is in units of Kelvin degrees. The effective temperatures are indicative of the air temperature at an altitude between 2 and 3 km. The small difference between  $T_u$  and  $T_d$  is due to the fact that the lower layers of the atmosphere have a greater influence on  $T_d$  than on  $T_u$ , and the higher layers have a greater influence on  $T_u$  than on  $T_d$ .

The sea-surface emissivity  $E$  consists of three components. The first component is the emissivity  $E_o$  for a specular (i.e., perfectly flat) sea surface. The second component is the change in emissivity  $\Delta E$  produced by sea-surface roughness and foam. This component is called the wind-induced emissivity and was originally derived from an analysis of collocated SeaSat microwave radiometer and scatterometer measurements [23]. The radiometer measurements gave  $T_B$  values, and the scatterometer measurements gave wind speed values. This  $T_B$  versus  $W$  data set provided the means to find a relationship between  $\Delta E$  and  $W$ . The SeaSat radiometer operated at an incidence angle of  $\theta_i = 49^\circ$ , and hence  $\Delta E$  was keyed to that incidence angle. To apply the brightness temperature model to other satellites, a third component to  $E$  is included. This component gives the variation of  $\Delta E$  with respect to  $\theta_i$ . The

sea-surface emissivity is then given by

$$E = E_o + \Delta E + \beta W(\theta_i - 49^\circ). \quad (7)$$

The specular emissivity is computed from the Fresnel equation [7], which is a function of polarization, incidence angle, and the dielectric constant  $\epsilon$  of sea water. The dielectric constant is a function of the radiation frequency, the water temperature, and the water salinity. At 37 GHz, the dependence on salinity is very small, and it is sufficient to assume a nominal value of 35 parts per thousand. Expressions for  $\epsilon$  are given by many investigators, notably [20], [11]. A review of these investigations found much disparity in the specification of  $\epsilon$ . There is clearly a need for new laboratory measurements using state-of-the-art technology and taken at satellite radiometer frequencies. However, based on the available data, much of which was taken in the 1940's and 1950's, it appears that the Stogryn and Klein-Swift expressions need to be modified, particularly above 10 GHz. Accordingly, we perform a least-squares analysis to rederive expressions for  $\epsilon$ . The analysis is somewhat subjective in that we exclude some data that appear to be anomalous. Using our best estimate of  $\epsilon$ , the following expression for the specular emissivity is obtained for incidence angles in the range  $51^\circ \pm 3^\circ$ .

$$E_o = \frac{(s_0 + s_1 t + s_2 t^2 + s_3 t^3 + s_4 q + s_5 t q + s_6 q^2 + s_7 t^2 q)}{T_s} \quad (8a)$$

$$t = T_s - 273.16 \quad (8b)$$

$$q = \theta_i - 51^\circ. \quad (8c)$$

The values for the  $s$  coefficients are given in Table I for the five lower SSM/I channels. The form for the wind-induced emissivity is derived by Wentz *et al.* [24] in (9a)–(9c) as

$$\begin{cases} \Delta E = m_1 W & \text{when } W \leq 7 & (9a) \\ \Delta E = m_1 W + (m_2 - m_1)(W - 7)^2 / W_a & \text{when } 7 < W \leq 17 & (9b) \\ \Delta E = m_2 W - W_b(m_2 - m_1) & \text{when } 17 < W. & (9c) \end{cases}$$

where  $W_a = 20$  m/s and  $W_b = 12$  m/s. Equation (9) represents two linear segments connected by a quadratic spline such that the first derivative in  $W$  is continuous. The values for  $m_1$  and  $m_2$  are given in Table I. These values are the same as those derived in [24] using the SeaSat data, except for horizontal polarization at 37 GHz. The 37H  $m_1$  and  $m_2$  values in Table I are about 10% higher than those originally derived from SeaSat. The 10% adjustment was made after comparisons of SSM/I winds (derived according to the algorithm presented herein) and the buoy winds showed that the SSM/I winds were consistently too high by about 10%. Considering the fact that the SeaSat radiometer suffered from considerable calibration problems, an error bracket of 10% on the original  $m$  coefficients is reasonable. Note that a linear interpolation in frequency is used to convert from the SeaSat frequencies of 18 and 21 GHz to the SSM/I frequencies of 19.35 and 22.235 GHz.

The third term in (7) models the incidence angle variation of  $\Delta E$ . The  $\beta$  coefficient, which is given in Table I, comes from [23]. A scaling factor of 4.697 is applied to the value in [23] in order to convert from the original friction-velocity notation to the wind-speed notation used herein. In [23], a linear relationship between friction velocity  $U_*$  and wind speed  $W$  was assumed, with  $U_* = 100$  cm/s corresponding to  $W = 21.29$  m/s. This same scaling factor is applied to the  $\omega$  coefficients in Table I.

The sea and air temperatures,  $T_s$  and  $T_a$ , are specified by climatology. We use Reynolds' [16] monthly sea-surface temperature tables that give  $T_s$  on a  $1^\circ$  latitude-longitude grid, and the assumption is made that  $T_a = T_s$ . For the wind speed retrievals done in the vicinity of the NDBC buoys,  $T_s$  and  $T_a$  are set to the values reported by the buoy rather than relying on climatology. The remaining parameter to be specified is the incidence angle  $\theta_i$ . This angle is computed from the known geometry of the SSM/I orbit.

Having specified  $F(W, \tau)$ , (3a) and (3b) are solved by Newton's method. The function  $F(W, \tau)$  is quasilinear in terms of  $W$  and  $\tau$ , and the following approximation is used:

$$F(W, \tau) \approx F(W_o, \tau_o) + (\partial F / \partial W)(W - W_o) + (\partial F / \partial \tau)(\tau - \tau_o). \quad (10)$$

The terms  $W_o$  and  $\tau_o$  are "first-guess" values for the wind and transmittance. Good choices are 8 m/s and 0.8, respectively, which represent typical values over the ocean. The final solution is independent of  $W_o$  and  $\tau_o$ , but the number of iterations is minimized by starting with typical values. The derivatives  $\partial F / \partial W$  and  $\partial F / \partial \tau$ , which are found by analytically differentiating the above equations, are evaluated at  $(W_o, \tau_o)$ . With this approximation, (3a) and (3b) become two linear equations with two unknowns,  $W$  and  $\tau$ . The system of equations is inverted to yield  $W$  and  $\tau$ . A second iteration is then done for which  $W_o$  and  $\tau_o$  are set to the wind and transmittance values coming from the first iteration. This procedure is repeated until the wind speed value converges. Convergence is defined as  $|W_n - W_{n-1}| < 0.05$  m/s, where  $W_n$  and  $W_{n-1}$  are the wind speeds computed on the  $n$  and  $n - 1$  iterations. Typically, convergence is obtained after 3

to 5 iterations. If convergence is not obtained in 10 iterations, then the brightness temperatures are flagged as anomalous. For SSM/I, nonconvergence occurs very rarely (less than 0.01% of the observations) and indicates either erroneous brightness temperatures or possibly heavy rain.

## V. DETECTION OF RAIN

The accuracy of the wind speed retrieval degrades when rain is present. The rain produces large variations in the atmospheric brightness temperature that overwhelm the small depolarization signal produced by the surface roughness. We do not attempt to retrieve wind speed in the presence of rain. Rain is detected by computing the liquid water absorption  $A_L$  at 37 GHz, as is discussed in this section.

The total absorption along the SSM/I viewing path is equal to  $\ln(1/\tau)$  and is the sum of three components: oxygen, water vapor, and liquid water (i.e., both cloud and rain water). It is convenient to normalize the absorption in terms of a vertically integrated quantity rather than a viewing-path integrated quantity. In this way, the dependence on incidence angle  $\theta_i$  is removed. For incidence angles below  $60^\circ$ , the ratio of the viewing-path length through the troposphere to the height of the troposphere is simply  $\sec \theta_i$ . The total absorption is then given by

$$\ln(1/\tau) = (A_O + A_V + A_L) \sec \theta_i \quad (11)$$

where  $A_O$ ,  $A_V$ , and  $A_L$  are the vertically integrated, or columnar, absorption components due to oxygen, water vapor, and liquid water, respectively.

To separate the liquid water signal from the water vapor signal, the transmittance is found at two frequencies, 22 and 37 GHz. The 37-GHz transmittance  $\tau_{37}$  is a by-product of the wind speed algorithm described in Section IV. The 22-GHz transmittance  $\tau_{22}$  is found by solving (3a) for 22 GHz. The wind speed in (3a) is set to the value derived from the 37 GHz channels. Equation (3a) is quadratic in terms of  $\tau_{22}$  and is easily solved. Table I gives the values for the 22-GHz model coefficients. There is one modification to the 22-GHz model that is not discussed above. Near the water vapor absorption line at 22.235 GHz, the radiosonde analysis shows that the effective air temperatures  $T_u$  and  $T_d$  depend on the water vapor content in the following way:

$$T_u = T_a - 11.0 - 7.2(V/V_o)^2 \quad (12a)$$

$$T_d = T_a - 10.2 - 3.4(V/V_o)^2 \quad (12b)$$

where  $V$  is the vertically integrated water vapor in columnar-density units of grams per squared centimeters, and  $V_o$  is a constant equaling  $6 \text{ g/cm}^2$ . Equation (12) is expressing the statistical property that the effective height of the water vapor column increases as the water vapor content  $V$  increases. An increase in the effective height produces a decrease in the effective air temperature relative to the surface temperature. At 37 GHz this effect is not appreciable, and the simpler form given by (6) is sufficient.

To determine the effective values for  $A_O$  and  $A_V$ , the radiosonde profiles in conjunction with Liebe's [13] oxygen and water vapor absorption coefficients are used to compute 609 sets of  $A_O$  and  $A_V$ . An analysis of these results shows that  $A_O$  is essentially constant except for a small dependence on air temperature and that  $A_V$  is approximately proportional to the vertically integrated water vapor  $V$ . The absorptions at 22 and 37 GHz are then approximated by the following expressions:

$$\ln(1/\tau_{22}) = (A_{O22} + \alpha_{V22}V + A_{L22}) \sec \theta_i \quad (13a)$$

$$\ln(1/\tau_{37}) = (A_{O37} + \alpha_{V37}V + A_{L37}) \sec \theta_i \quad (13b)$$

$$A_{O22} = 0.01372[1 - 0.0058(T_a - 288)] \quad (14a)$$

$$A_{O37} = 0.04093[1 - 0.0057(T_a - 288)]. \quad (14b)$$

The water vapor coefficients  $\alpha_{V22}$  and  $\alpha_{V37}$  are  $0.062 \text{ cm}^2/\text{g}$  and  $0.020 \text{ cm}^2/\text{g}$ , respectively. Equations (13a) and (13b) represent two equations in three unknowns:  $V$ ,  $A_{L22}$ , and  $A_{L37}$ . To solve the equations, it is necessary to assume some relationship between the liquid water absorption at 22 and 37 GHz. For cloud droplets, which are very small compared to the radiation wavelengths being considered, the following Rayleigh scattering relationship holds:

$$A_{L22} = 0.37507 A_{L37}. \quad (15)$$

Mie scattering computations show that this relationship is valid for light rain not exceeding about 2 mm/h. For heavier rain, the 0.37507 coefficient begins to increase. Given  $\tau_{22}$  and  $\tau_{37}$ , equations (13), (14) and (15) are then solved, yielding  $V$ ,  $A_{L22}$ , and  $A_{L37}$ .

Wentz [26] did 38 case studies of storms in the Northeast Pacific. Images of  $A_{L37}$  were compared with GOES infrared and visible images, 500 mb and 850 mb analyses, and rain gauge reports. These case studies indicate that the onset of rain (i.e., a light drizzle) is typically associated with a liquid water absorption near 0.044 napers. Accordingly, for the buoy versus SSM/I wind comparisons presented below, the SSM/I overpass is excluded if  $A_{L37}$  exceeds 0.044 napers.

In addition to the liquid water absorption, the rain detection algorithm also gives values for the columnar water vapor  $V$ . To validate this component of the algorithm, we compute SSM/I water vapor values in the vicinity of 575 radiosonde flights. These radiosonde data were compiled by Alishouse *et al.* [1]. Fig. 1 shows the SSM/I water vapors plotted versus the radiosonde values. The rms difference between the SSM/I and radiosonde water vapor contents is  $0.31 \text{ g/cm}^2$ , and there is no bias.

## VI. COMPARISON OF SSM/I AND BUOY WIND SPEEDS

For each of the 3831 buoy data sets, a wind speed  $W$  and liquid water absorption  $A_L$  are computed from the collocated SSM/I brightness temperatures. Out of this total, 500 sets have a value of  $A_L$  that exceeds 0.044 napers, and these sets are

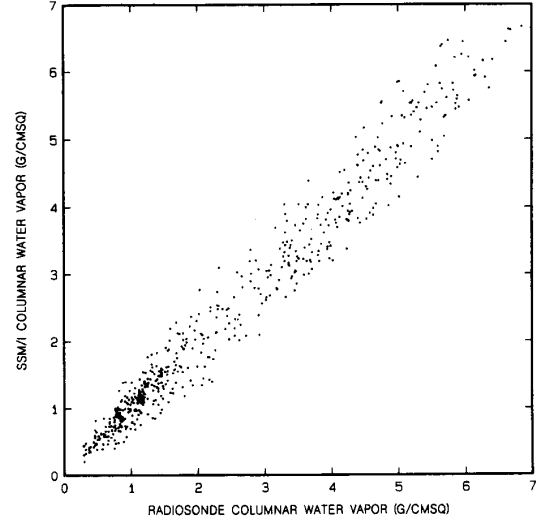


Fig. 1. A comparison of SSM/I columnar water vapor with the vertically integrated water vapor density obtained from radiosonde flights. The rms difference for the 575 comparisons is  $0.31 \text{ g/cm}^2$ .

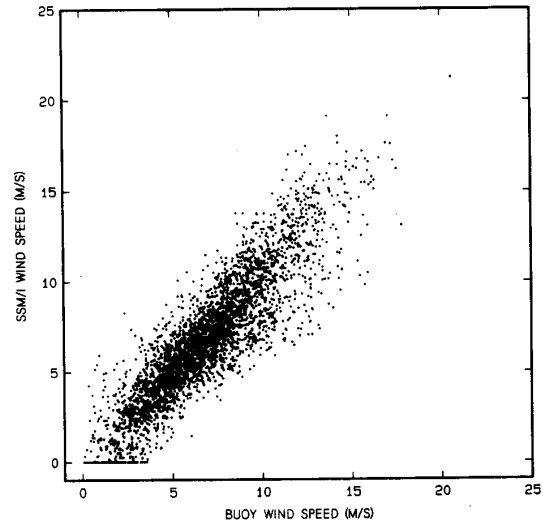


Fig. 2. A comparison of NDBC buoy wind speeds with those retrieved from the SSM/I 37-GHz observations. No correction is made for wind direction. The rms wind speed difference for the 3321 comparisons is 1.6 m/s.

excluded from further processing. Next, we excluded those sets for which the absolute difference between the SSM/I and buoy wind speed exceeds 6 m/s. There are ten such sets, which represent 0.3% of the total sets. Fig. 2 is a scatter plot of the remaining 3321 pairs of SSM/I and buoy wind speeds. The rms difference between the SSM/I and buoy wind speed is 1.59 m/s, and there is no bias. The correlation coefficient ( $r^2$ ) is 0.80. Note that the wind speeds coming from the SSM/I algorithm are referenced to an anemometer height of 19.5 m, while the buoy wind speeds are referenced to a 10 m height. To compare the two estimates of wind speed, the SSM/I wind speeds are reduced by 6%.

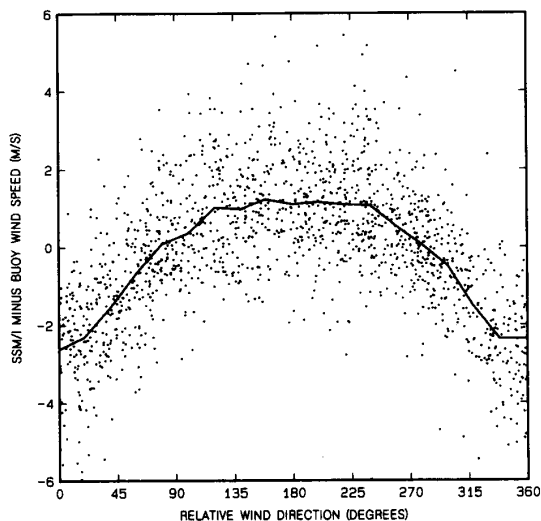


Fig. 3. The difference of the SSM/I wind speed minus the buoy wind speed plotted versus the relative wind direction. The solid curve is the average value of the individual points.

To detect a possible wind direction effect, we stratify the data according to the relative wind direction  $\phi_r$ , which is defined as the buoy wind direction  $\phi_w$  minus the SSM/I azimuth angle  $\phi$ . When  $\phi_r = 0^\circ$  ( $180^\circ$ ), the SSM/I is looking directly into (away from) the wind. Crosswind observations occur when  $\phi_r = 90^\circ$  and  $270^\circ$ . Fig. 3 shows the SSM/I minus buoy wind speed difference  $\Delta W$  plotted versus  $\phi_r$ . Only cases in which the buoy wind speed exceeds 7 m/s are shown. There is an obvious correlation between  $\Delta W$  and  $\phi_r$ . When SSM/I is looking upwind,  $\Delta W$  is about  $-2.5$  m/s as compared to the downwind value of  $+1.2$  m/s. The solid curve in Fig. 3 is the mean value of  $\Delta W$  computed for  $20^\circ$   $\phi_r$  bins. The correlation between  $\Delta W$  and  $\phi_r$  is less evident for winds below 7 m/s.

#### VII. DEPENDENCE OF BRIGHTNESS TEMPERATURE ON WIND DIRECTION

To determine the cause of the correlation of  $\Delta W$  with  $\phi_r$ , we analyze the dependence of  $T_B$  on  $\phi_r$ . To see this wind direction dependence, it is necessary to remove the variations due to the other geophysical parameters. The buoy data set provides the values for  $T_a$ ,  $T_s$ , and  $W$ . The remaining two parameters are the columnar water vapor and the liquid water absorption. Values for  $V$  and  $A_L$  are obtained from the SSM/I observations, as is discussed below. The following brightness temperature difference is then computed

$$\Delta T_B = T_B - F(W, V, A_L) \quad (16)$$

where  $T_B$  is the observed brightness temperature and  $F()$  is the radiative transfer function given by (4) and (13). The residual  $\Delta T_B$  is the brightness temperature component due to wind direction effects, measurement noise, and geophysical modeling errors.

If the algorithm described in Section V were used to find water vapor and liquid water absorption, then the  $V$  and  $A_L$

values would have a small error due to neglecting the wind direction effect. If these values were then used in (16) to remove the atmospheric variation, the wind direction error would be folded back into the statistics, and the results would be distorted. To avoid this aliasing problem, we use an alternate algorithm for which the inputs are the following brightness temperature differences:

$$t_1 = T_{B19v} - T_{B22v} \quad (17a)$$

$$t_2 = T_{B37v} - T_{B22v} \quad (17b)$$

$$t_3 = T_{B37h} - T_{B19h} \quad (17c)$$

The assumption is made that the wind direction signature  $\Delta T_B$  does not vary significantly over the 19 to 37-GHz band. The validity of this assumption is discussed below. Under this assumption,  $t_1$ ,  $t_2$ , and  $t_3$  are independent of the wind direction. Values for  $V$  and  $A_L$  are found such that the following sum of squares (SOS) is minimized

$$\text{SOS} = (t_1 - f_1)^2 + (t_2 - f_2)^2 + (t_3 - f_3)^2 \quad (18)$$

$$f_1 = F_{19v}(W, V, A_{L19}) - F_{22v}(W, V, A_{L22}) \quad (19a)$$

$$f_2 = F_{37v}(W, V, A_{L37}) - F_{22v}(W, V, A_{L22}) \quad (19b)$$

$$f_3 = F_{37h}(W, V, A_{L37}) - F_{19h}(W, V, A_{L19}). \quad (19c)$$

The Rayleigh scattering assumption is used to interrelate  $A_{L19}$ ,  $A_{L22}$ , and  $A_{L37}$ . As compared to the standard algorithm, the alternate algorithm results in larger errors in  $V$  and  $A_L$  because information on the magnitude of the brightness temperature is lost. However, it is preferable to have larger errors that are independent of wind direction than smaller errors that are correlated with wind direction.

Fig. 4 shows the values of  $\Delta T_B$  for the 3321 buoy data sets plotted versus the relative wind direction  $\phi_r$ . Vertical and horizontal polarizations are shown for three wind speed ranges: 0 to 6 m/s, 6 to 10 m/s, and over 10 m/s. The mean wind speeds corresponding to these three ranges are 3.9, 7.9, and 12.2 m/s. For each wind speed range, the  $\Delta T_B$  values are averaged into  $20^\circ$   $\phi_r$  bins, and these averages are shown by the X's. Each bin contains about 50 samples. The results for 19 and 37 GHz are essentially the same due to the way in which  $V$  and  $A_L$  are computed, and Fig. 4 shows the 37-GHz results. In view of Fig. 4, the wind direction dependence is empirically modeled by a second-order harmonic expansion.

$$\Delta T_B = B_1 \cos \phi_r + B_2 \cos 2\phi_r. \quad (20)$$

For each wind speed range, the coefficients  $B_1$  and  $B_2$  are found from least-squares fits, which are shown by the solid curves in Fig. 4. To better determine the wind speed variation of  $B_1$  and  $B_2$ , the number of wind speed bins is increased to six. The  $B_1$  and  $B_2$  values for these six bins are shown in Fig. 5 by the O's and X's, respectively. In view of Fig. 5, the wind speed dependence is modeled by

$$B_i = b_{1i}W + b_{2i}W^2 \quad (21)$$

where subscript  $i = 1$  and 2. The solid and dashed lines in Fig. 5 are the least-squares fits of (21) to the six data points, and

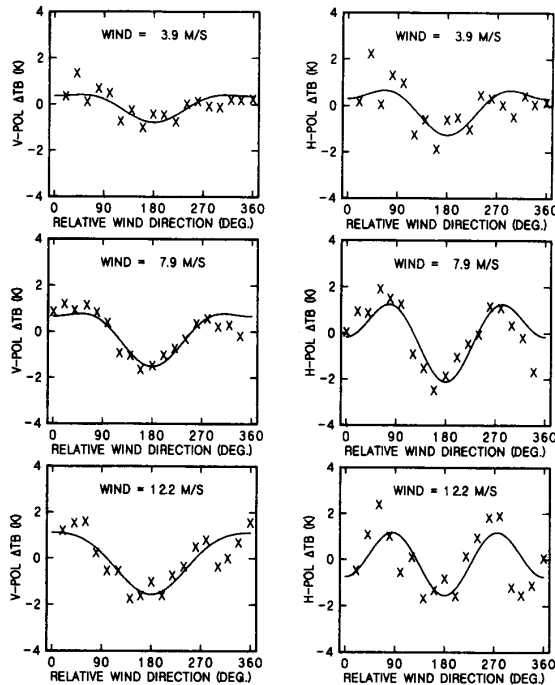


Fig. 4. The variation of brightness temperature with wind direction for three different wind speeds and two polarizations. The results for 19 and 37 GHz are essentially the same, and the 37-GHz results are shown here. The solid curves are second-order harmonic fits.

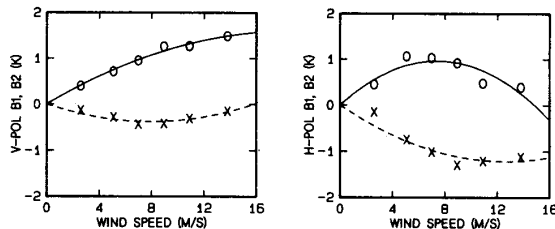


Fig. 5. The variation of the  $T_B$  wind direction signal with wind speed for both v-pol and h-pol. The O's show the dependence of the first-order harmonic on wind speed, and the X's show the dependence of the second-order harmonic. The curves are quadratic least-squares fits.

Table II gives the regression coefficients  $b_{1i}$  and  $b_{2i}$ . In Fig. 4, the data scatter of the v-pol  $\Delta T_B$  is highly correlated with the h-pol data scatter. This correlation suggests that much of the data scatter may be a result of the error in specifying  $V$  and  $A_L$ . To investigate this possibility,  $V$  and  $A_L$  are recomputed using just the 22V and 37V brightness temperatures. To do this, the v-pol wind direction signal  $\Delta T_B$  is computed using the coefficients in Table II. In doing this computation, the wind speed is set to the value reported by the buoy. Then, the computed  $\Delta T_B$  is subtracted from the 22V and 37V brightness temperature measurements to obtain  $T_B$  values that are less dependent on wind direction. These  $T_B$  values are then used by the algorithm described in Sections IV and V to obtain  $V$  and  $A_L$ . In this case, the 37H channel is not required because the wind speed in the algorithm is set to the buoy value. The

TABLE II  
COEFFICIENTS FOR  $T_B$  WIND DIRECTION SIGNAL

Coeff.	Units	V-pol	H-pol
$b_{11}$	$K s m^{-1}$	1.70E-1	2.60E-1
$b_{21}$	$K s^2 m^{-2}$	-0.44E-2	-1.75E-2
$b_{12}$	$K s m^{-1}$	-0.97E-1	-1.94E-1
$b_{22}$	$K s^2 m^{-2}$	0.61E-2	0.77E-2

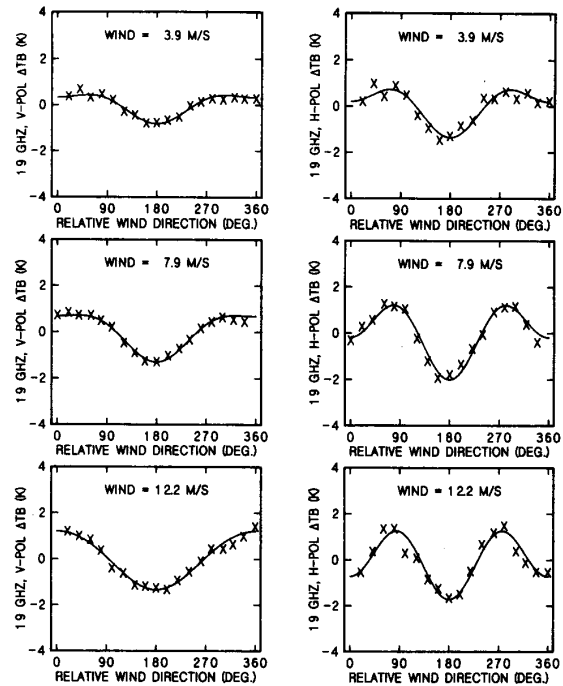


Fig. 6. Same as Fig. 4 except that the 19-GHz results are shown and an additional correction to remove the atmospheric interference is applied.

values of  $V$  and  $A_L$  coming from this second iteration should be more accurate because information on the magnitude of  $T_B$  is retained, and the error that is correlated with wind direction should be small because the first-order estimate of the wind direction signal  $\Delta T_B$  has been removed. The wind direction signal is recomputed using the new estimates of  $V$  and  $A_L$ . Fig. 6 shows the values of the recomputed  $\Delta T_B$  for the 19-GHz vertical and horizontal polarization channels. The data scatter has been substantially reduced by using the new estimates of  $V$  and  $A_L$ . Fig. 7 shows the analogous results for the 37-GHz vertical and horizontal polarization channels. The 19 and 37-GHz  $\Delta T_B$ 's are very similar, and the assumption that  $\Delta T_B$  is invariant over the 19 to 37-GHz band appears to be valid. By necessity, the 22 and 37-GHz v-pol  $\Delta T_B$  perfectly fit the wind direction signature specified by Table II because these channel are used to derive the  $V$  and  $A_L$  values.

We conclude this section by recomputing the SSM/I wind speed values, this time taking into account the wind direction effect. The coefficients in Table II are used to compute  $\Delta T_B$ , which is then subtracted from the 37-GHz v-pol and h-pol  $T_B$  observations. The corrected  $T_B$  observations are



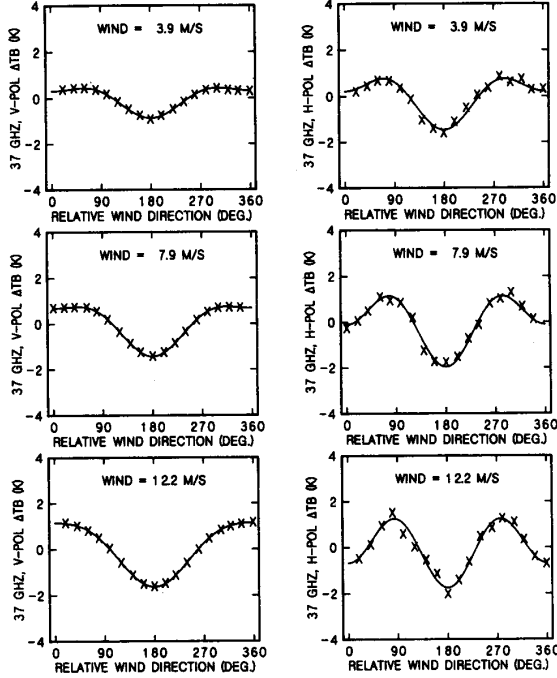


Fig. 7. Same as Fig. 4 except that an additional correction to remove the atmospheric interference is applied.

then processed by the algorithm described in Section IV. Fig. 8 shows the resulting scatter plot of SSM/I winds versus buoy winds. Comparing Fig. 8 with Fig. 2 clearly shows an improvement. The rms difference and correlation coefficient ( $r^2$ ) are now 1.29 m/s and 0.85 as compared to 1.59 m/s and 0.80 for the uncorrected winds. The correction for wind direction removes many of the outlying data points. The number of sets for which the absolute difference between the SSM/I and buoy wind speed exceeds 6 m/s is reduced from 10 to 4. Considering the spatial mismatch between the buoy and satellite observations, one does not expect to do much better than 1.3 m/s.

#### VIII. SSM/I MONTHLY WIND VECTOR MAPS

In this section, we try to retrieve both wind speed and direction from SSM/I observations. The computation of wind direction requires observations of the same ocean area taken at different azimuth angles. In addition, it is necessary to separate the wind signal from the atmospheric signal. Our approach to this problem is to sort the SSM/I observations into  $5^\circ$ -latitude by  $10^\circ$ -longitude by 1-month bins. Each bin then contains observations over a wide range of azimuth angles. The azimuth angles for the descending orbit segments range from  $-40^\circ$  to  $60^\circ$ , and the angles for the ascending segments range from  $120^\circ$  to  $220^\circ$ . Typically a given bin contains about 30 000 multichannel observations. We assume that this sample size is large enough so that the correlation between the atmosphere and the wind signal will tend to zero when doing the averages discussed below. To further reduce the atmospheric interference, the following linear combination of

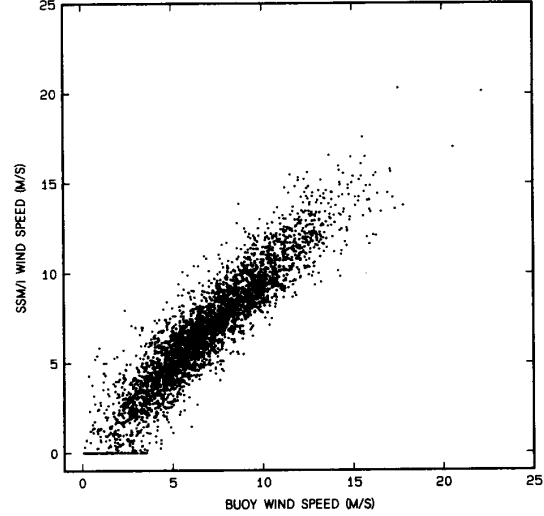


Fig. 8. Same as Fig. 2 except that a correction for wind direction is applied. The rms wind speed difference is now 1.3 m/s.

the v-pol and h-pol 19-GHz observations is used for the wind vector retrieval:

$$T_{Bx} = T_{Bv} - 0.52T_{Bh}. \quad (22)$$

The 19-GHz channels are chosen because they are least affected by the atmosphere, and the linear combination of polarizations is particularly insensitive to atmospheric variations. The results in the last section indicate that  $T_{Bx}$  has the form

$$T_{Bx} = T_{Bx0} + B_{x1} \cos \phi_r + B_{x2} \cos 2\phi_r \quad (23)$$

$$B_{xi} = B_{vi} - 0.52B_{hi}. \quad (24)$$

where subscript  $i = 1$  and 2. The term  $T_{Bx0}$  is the average of  $T_{Bx}$  over  $\phi_r$ . Over the  $5^\circ$  by  $10^\circ$  ocean area,  $T_{Bx0}$  can have small systematic variations that are correlated with latitude and longitude. One example is the strong correlation of water vapor with latitude. These variations in  $T_{Bx0}$  can introduce errors into the wind vector estimation. To correct for this effect, a monthly  $1^\circ$ -latitude by  $1^\circ$ -longitude map of  $T_{Bx}$  is made. This monthly average is then subtracted from each  $T_{Bx}$  observation to obtain the quantity

$$T'_{Bx} = T_{Bx0} - (T_{Bx})_{\text{map}} + B_{x1} \cos \phi_r + B_{x2} \cos 2\phi_r \quad (25)$$

where the prime sign ' on  $T_{Bx}$  denotes that the monthly map component  $(T_{Bx})_{\text{map}}$  has been subtracted. In doing this correction, the monthly map value is interpolated to the exact location of the observation.

Table II shows that the coefficient  $B_{x1} = 0.035W + 0.0047W^2$ , which can be approximated by  $B_{x1} = 0.09W$  to a rms accuracy of 0.1 K over the range from 0 to 15 m/s. Using this approximation and noting that  $\phi_r = \phi_w - \phi$ , (25) becomes

$$T'_{Bx} = T_{Bx0} - (T_{Bx})_{\text{map}} + 0.09(u \sin \phi + v \cos \phi) + O(2\phi) \quad (26)$$

$$u = W \sin \phi_w \quad (27a)$$

$$v = W \cos \phi_w \quad (27b)$$

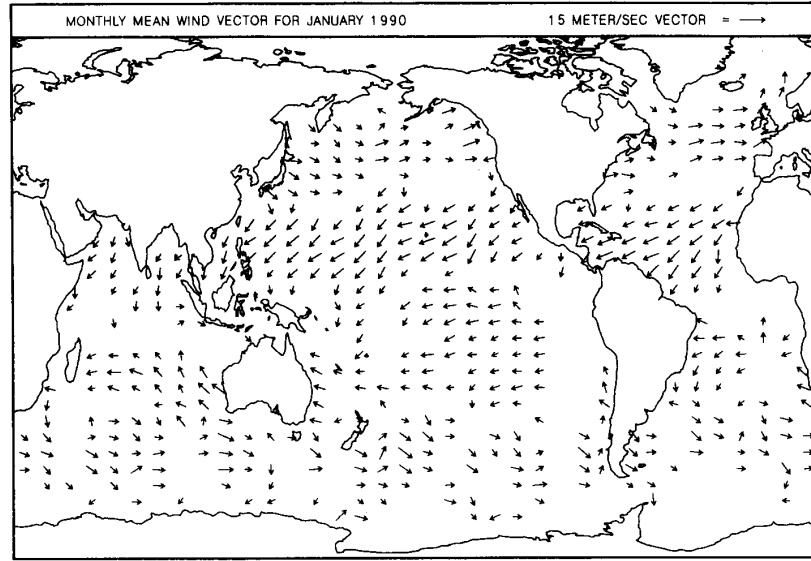


Fig. 9. Monthly mean wind vector for January 1990 as derived from SSM/I.

where  $u$  and  $v$  are the zonal and meridional components of the wind. The last term  $O(2\phi)$  denotes the second-order harmonics, i.e., the  $B_{x2}$  terms.

The quantities  $T'_{Bx}$  are sorted into  $3.2^\circ$  azimuth angle bins and then averaged. The  $3.2^\circ$  bin corresponds to two adjacent observations along the SSM/I scan. Let  $\langle \rangle_k$  denote the average over the monthly  $5^\circ$  by  $10^\circ$  bin for those azimuth angles in the range  $\phi_k \pm 1.6^\circ$ . Averaging (26) gives

$$\begin{aligned} \langle T'_{Bx} \rangle_k = & \langle T_{Bx0} - (T_{Bx})_{map} \rangle_k \\ & + 0.09 \left( \langle u \rangle_k \sin \phi_k + \langle v \rangle_k \cos \phi_k \right) + \langle O(2\phi) \rangle_k. \end{aligned} \quad (28)$$

The assumption is made that the monthly  $5^\circ$  by  $10^\circ$  average of the zonal and meridional wind is the same for all SSM/I azimuth angle bins. This assumption of spatial uniformity of the monthly averages is expressed by  $\langle u \rangle_k = \langle u \rangle$  and  $\langle v \rangle_k = \langle v \rangle$ . The monthly averages  $\langle u \rangle$  and  $\langle v \rangle$  are found from a least-squares fit in which  $\langle T'_{Bx} \rangle_k$  represents 64 observations (i.e., 32 observations over a SSM/I scan for ascending orbit segments and another 32 observations for descending orbit segments). The coefficients  $\sin \phi_k$  and  $\cos \phi_k$  are known, and the unknowns are  $\langle u \rangle$  and  $\langle v \rangle$ . The term  $\langle T_{Bx0} - (T_{Bx})_{map} \rangle$  represents noise, and results show that its rms value is typically about 0.3 K.

The effect of the second-order term  $\langle O(2\phi) \rangle_k$  on the estimation of  $\langle u \rangle$  and  $\langle v \rangle$  is small for two reasons. First, the magnitude of  $B_{x2}$  is about 25% of that for  $B_{x1}$ . Second, if observations were available for all  $\phi_k$ , then the estimation of the amplitudes of the  $\cos \phi_k$  and  $\sin \phi_k$  terms would not depend on whether or not the model contains higher order terms. For our case,  $\phi_k$  covers much of the full  $360^\circ$  range, thereby making the effect of the second-order terms small.

Least-squares fits are done for both cases (i.e., including and excluding the second-order terms), and similar results are obtained. For the results to be presented, the term  $\langle O(2\phi) \rangle_k$  is not included when doing the fits.

The zonal and meridional wind components are shown in Figs. 9 and 10 for January and July, 1990, respectively. The two maps show  $\langle u \rangle$  and  $\langle v \rangle$  as a vector that points in the direction of flow. Areas void of vectors represent regions where the mean wind speed as computed from either the vector or scalar average is less than 4 m/s. Also, areas close to land and sea ice are excluded. Each vector is computed from an independent set of SSM/I observations, and there has been no editing or smoothing. There do appear to be some errant vectors that need correcting. However, the large-scale features of the global circulation are apparent. The trade winds, the westerlies, and the rotation about the subtropical highs are clearly delineated. In January, the monsoon in the Arabian Sea is out of the Northeast, and there are strong westerlies in the North Pacific and North Atlantic. In July, the Arabian monsoon reverses direction, and the westerlies in the Northern Hemisphere diminish.

Our primary objective in producing these initial maps is to verify that there is indeed a wind direction signal in the brightness temperatures. The maps confirm this assertion. However, we emphasize that the maps are a "first-look" product, and considerably more work is needed in order to determine their scientific usefulness.

## IX. SIMULATION OF A TWO-LOOK RADIOMETER

We finally investigate the possibility using a two-look radiometer to retrieve wind vectors along the satellite swath. An example of a two-look radiometer is an SSM/I that is mounted on the spacecraft so that it can see in both the forward and aft direction. For this configuration, the ocean

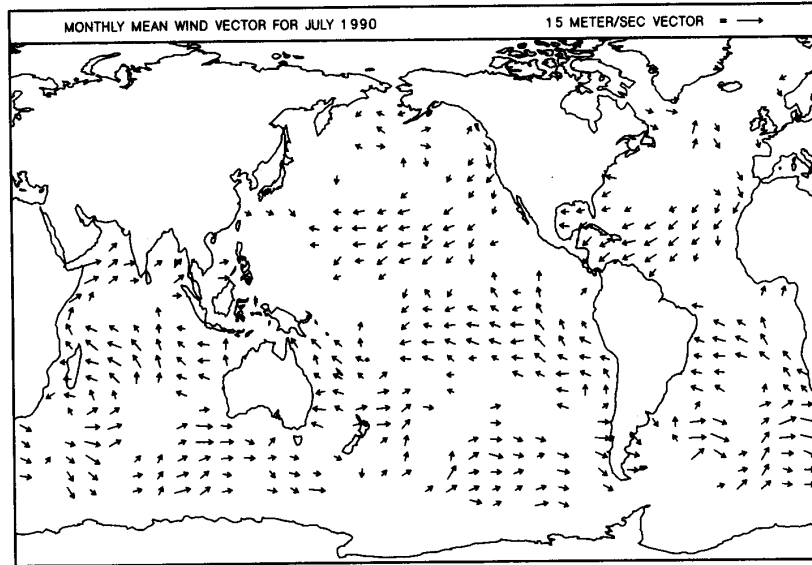


Fig. 10. Monthly mean wind vector for July 1990 as derived from SSM/I.

surface is first seen during the forward-looking portion of the scan. Then, about 4 min later the same area is seen during the aft-looking portion of the scan. An alternative design is to have two SSM/I's, one on the bow of the spacecraft and the other on the stern. The formulation for this problem is simplified by expressing the observation and wind azimuth angles,  $\phi$  and  $\phi_w$ , relative to the direction of the satellite subtrack. In this coordinate system,  $\phi_w = 0$  represents a wind blowing toward the oncoming satellite. An ocean cell observed at the azimuth angle  $\phi$  during the forward scan is later seen at the azimuth angle  $180^\circ - \phi$  during the aft scan. Assuming the wind direction dependence given by (20), the difference between the forward minus aft observations is

$$T_{Bf} - T_{Ba} = 2B_1 \cos \phi \cos \phi_w + 2B_2 \sin 2\phi \sin 2\phi_w. \quad (29)$$

The  $B$  coefficients depend on wind speed, which can be found from the wind speed algorithm discussed in Section IV. When computing the wind speed, the sum of the two observations is used. Considering both polarizations, (29) represents two linear equation with two unknowns denoted by  $X = \cos \phi_w$  and  $Y = \sin 2\phi_w$ . The v-pol and h-pol equations are inverted to obtain values for  $X$  and  $Y$ , and then the wind direction angle  $\phi_w$  is found from the following expression:

$$\phi_w = \arctan(Y/2X, X). \quad (30)$$

When  $X = 0$ , there are two possible solutions:  $\phi_w = 90^\circ$  and  $270^\circ$ . For all other values, (30) uniquely gives  $\phi_w$ . In other words, the wind direction can be uniquely found except for the case in which the wind is blowing exactly perpendicular to the subtrack. For this crosswind case there are two possible solutions: blowing from either the port or starboard.

Observation noise and modeling errors will, of course, degrade the estimation of  $\phi_w$ . The effect of these errors on the  $\phi_w$  retrieval is assessed by doing a computer simulation.

The radiometer rms noise is assumed to be 0.3 K, which corresponds to the SSM/I value. The modeling error is assumed to have a 20% systematic component and a 20% random component and is characterized by

$$\hat{B}_i = (1 + \delta_1 + \delta_2)B_i \quad (31)$$

where subscript  $i = 1$  and 2. The terms  $\delta_1$  and  $\delta_2$  are Gaussian noise having a rms value of 0.2. A value for the systematic noise  $\delta_1$  is generated once each scan, and a value for the random noise  $\delta_2$  is generated at each scan position. The modeling noise is generated separately for the two polarizations.

A simplistic wind field with a constant wind speed is assumed. Three wind speed cases are considered: 5, 10, and 15 m/s. The wind direction has an alongscan gradient of  $20^\circ$  per 100 km. In addition, at each scan position a random component having a rms variation of  $10^\circ$  is added to the smoothly varying wind direction. A total of 360 wind direction cases is considered. These cases correspond to incrementing the wind direction at the center of the scan by  $1^\circ$  over the range from  $0^\circ$  to  $359^\circ$ .

The retrieval algorithm divides the SSM/I scan in half and assumes that over each half (i.e., port and starboard) the wind direction varies as

$$\phi_w = \phi_{wo} + \xi x \quad (32)$$

where  $\phi_{wo}$  is the wind direction at the center of the scan and  $x$  is the alongscan distance measured from the scan center. The wind direction gradient  $\xi$  is assumed constant over the half scan. The scan halves are treated independently, and for each half the algorithm finds values for  $\phi_{wo}$  and  $\xi$ . These values are found so as to minimize the sum of squares (SOS) in (33) at the top of the next page. The summation is over both polarizations and the 33 scan positions in a half scan.

$$\text{SOS} = \sum [T_{Bf} - T_{Ba} - 2\hat{B}_1 \cos \phi \cos(\phi_{wo} + \xi x) - 2\hat{B}_2 \sin 2\phi \sin(2\phi_{wo} + 2\xi x)]^2. \quad (33)$$

The SOS can have several local minima in  $(\phi_{wo}, \xi)$  space. These minima correspond to multiple solutions that occur because of the inclusion of noise. A search is performed to locate these minima. In most cases, the correct solution is the minima that has the smallest SOS. For the 5-m/s wind speed case, the minima with the smallest SOS is the correct solution 97.4% of the time. For the 10-m/s and 15-m/s wind speed cases, the minima with the smallest SOS is the correct choice 99.3% and 99.8% of the time, respectively. The remainder of the time, the minima with the second smallest SOS is the correct choice, while the minima with the smallest SOS corresponds to a wind direction that is  $360^\circ$  minus the true wind direction. The values for  $\phi_{wo}$  and  $\xi$  corresponding to the correct minima are then substituted into (32) in order to find the wind direction along the scan. The retrieved wind direction is compared to the true direction, and the rms difference is typically about  $15^\circ$ . The existence of multiple wind direction solutions and the searching procedure to find SOS minima have their counterparts in the wind vector retrieval problem for scatterometers [27].

The fact that the true wind direction varies along the scan helps to reduce the problem of multiple solutions. For example, the most serious multiple solution problem occurs when the wind direction is exactly perpendicular to the subtrack. In this case, (30) has two distinct solutions, as mentioned above. However, we have assumed that the wind direction varies along the scan, and hence the crosstrack wind condition will occur for only for a portion of the scan. For example, if the wind direction is perpendicular to the subtrack at the scan center, then it will be aligned with the subtrack near the scan edge. A second set of simulations is done in which the true wind direction is assumed constant over the swath except for the  $10^\circ$  random component. In these simulations the multiple-solution problem is worst, particularly for the crosstrack wind cases of  $\phi_w = 90^\circ \pm 10^\circ$  and  $\phi_w = 270^\circ \pm 10^\circ$ . For this range of angles, the two solutions:  $\phi_w \approx 90^\circ$  and  $\phi_w \approx 270^\circ$  have approximately equal likelihood of being the correct choice. In the actual operation of an orbiting spacecraft, this crosstrack wind condition will occur only for a short segment of the orbit, and the  $180^\circ$  ambiguity can probably be resolved by looking at the retrieved wind field on either side of the area having the crosstrack wind. Excluding those cases for which  $\phi_w = 90^\circ \pm 10^\circ$  and  $\phi_w = 270^\circ \pm 10^\circ$ , the minima with the smallest SOS is the correct choice 90.6%, 96.3%, and 99.7% of the time for the 5 m/s, 10 m/s, and 15 m/s wind speeds, respectively. The rms wind direction error is again about  $15^\circ$ .

## X. CONCLUSIONS

The microwave emission from the ocean has an appreciable dependence on wind direction. This conclusion is supported by the plots of  $T_B$  versus buoy wind direction and by the

maps of the monthly mean wind vector. The newly found wind direction signal now needs to be better characterized. Herein, our *in situ* data base is limited to 3321 buoy reports during the first 9 months of SSM/I operation. Now that SSM/I has been in operation for 4 years, it is possible to obtain about 30 000 collocated buoy-SSM/I observations. This large data base should be compiled in order to better determine the directional signal and its associated variability.

Another issue that needs clarification is the scientific utility of the monthly SSM/I wind vector maps. The accuracy and usefulness of this new low-resolution product need to be examined. The maps should be compared with other available sources of information such as monthly wind fields coming from numerical models. The wind fields to be derived from the scatterometers on the European ERS-1 and Japanese ADEOS satellites will also be useful for intercomparisons.

Finally, the simulations of the two-look radiometer need to be expanded. Realistic wind fields for a variety of mesoscale features should be considered, and various radiometer configurations should be tested. These simulations will determine the feasibility of obtaining mesoscale wind fields from satellite microwave radiometers.

## ACKNOWLEDGMENT

We wish to thank J. Wilkerson at NOAA/NESDIS for supplying the Level-1 SSM/I data tapes. In addition, we are grateful to M. Goodberlet and C. Swift at the University of Massachusetts for providing the NDBC data and to J. Alishouse at NOAA/NESDIS for providing the radiosonde data.

## REFERENCES

- [1] J. C. Alishouse, S. A. Snyder, J. Vongsathorn, and R. R. Ferraro, "Determination of oceanic total precipitable water from the SSM/I," *IEEE Trans. Geosci. Remote Sensing*, vol. 28, pp. 811-816, 1990.
- [2] Ye. A. Bespalova, V. M. Veselov, V. Ye. Gershenson *et al.*, "Determining surface wind velocity by measurements of polarization anisotropy of natural and scattered microwave radiation," *Issledovaniye Zemli Iz Kosmosa*, pp. 87-94, 1982.
- [3] C. S. Cox, "Measurements of slopes of high-frequency wind waves," *J. Mar. Res.*, vol. 16, pp. 199-225, 1958.
- [4] C. S. Cox and W. H. Munk, "Measurement of the roughness of the sea surface from photographs of the sun's glitter," *J. Opt. Soc. Am.*, vol. 44, pp. 838-850, 1954.
- [5] M. A. Goodberlet, C. T. Swift, and J. C. Wilkerson, "Remote sensing of ocean surface winds with the Special Sensor Microwave/Imager," *J. Geophys. Res.*, vol. 94(C10), pp. 14 547-14 555, 1989.
- [6] J. P. Hollinger, "DMSP Special Sensor Microwave/Imager calibration/validation," NRL Tech. Rep., Naval Research Laboratory, Washington, DC, July 1989.
- [7] J. D. Jackson, *Classical Electrodynamics*. New York: John Wiley & Sons, Inc., 1962, pp. 216-220.
- [8] W. L. Jones, L. C. Schroeder, and J. L. Mitchell, "Aircraft measurements of the microwave scattering signature of the ocean," *IEEE J. Oceanic Eng.*, vol. OE-2, p. 52, 1977.

- [9] W. L. Jones, P. G. Black, D. M. Boggs, E. M. Bracalente, R. A. Brown, G. Dome, J. A. Ernst, I. M. Halberstam, J. E. Overland, S. Petcherych, W. J. Pierson, F. J. Wentz, P. M. Woiceshyn, and M. G. Wurtele, "Seasat scatterometer: Results of the Gulf of Alaska workshop," *Science*, vol. 204(4400), pp. 1413-1415, 1979.
- [10] W. C. Keller, and J. W. Wright, "Microwave scattering and the straining of wind-generated waves," *Radio Sci.*, vol. 10, pp. 139-147, 1975.
- [11] L. A. Klein and C. T. Swift, "An improved model for the dielectric constant of sea water at microwave frequencies," *IEEE J. Oceanic Eng.*, vol. OE-2, pp. 104-111, 1977.
- [12] Yu. A. Kravtsov, Ye. A. Mirovskaya, A. Ye. Popov *et al.*, "Critical phenomena accompanying thermal radiation of periodically uneven water surface," *Izv. An SSSR: Ser. Fizika Atmosfery i Okeana*, vol. 14, no. p. 7, (New of the USSR Academy of Sciences: Physics of the Atmosphere and Ocean), pp. 733-739, 1978.
- [13] H. J. Liebe, "An updated model for millimeter wave propagation in moist air," *Radio Sci.*, vol. 20, no. 5, pp. 1069-1089, 1985.
- [14] H. Mitsuyasu, and T. Honda, "Wind-induced growth of water waves," *J. Fluid Mech.*, vol. 123, pp. 425-442, 1982.
- [15] E. C. Monahan and I. O'Muircheartaigh, "Optimal power-law description of oceanic whitecap coverage dependence on wind speed," *J. Phys. Oceanogr.*, vol. 10, pp. 2094-2099, 1980.
- [16] R. W. Reynolds, "A monthly averaged climatology of sea surface temperature," NOAA Tech. Rep. NWS 31, National Weather Service, Silver Spring, MD, 1982.
- [17] S. O. Rice, "Reflection of electromagnetic waves from slightly rough surfaces," *Commun. Pure Appl. Math.*, vol. 4, pp. 351-378, 1951.
- [18] P. M. Smith, "The emissivity of sea foam at 19 and 37 GHz," *IEEE Trans. Geosci. Remote Sensing*, vol. GE-26, pp. 541-547, 1988.
- [19] A. Stogryn, "The apparent temperature of the sea at microwave frequencies," *IEEE Trans. Antennas Propagat.*, vol. AP-15, pp. 278-286, 1967.
- [20] A. Stogryn, "Equations for calculating the dielectric constant of saline water," *IEEE Trans. Microwave Theory Tech.*, vol. MTT-19, pp. 733-736, 1971.
- [21] A. Stogryn, "The emissivity of sea foam at microwave frequencies," *J. Geophys. Res.*, vol. 77, pp. 1650-1666, 1972.
- [22] F. J. Wentz, "A two-scale scattering model for foam-free sea microwave brightness temperatures," *J. Geophys. Res.*, vol. 80, pp. 3441-3446, 1975.
- [23] F. J. Wentz, "A model function for ocean microwave brightness temperatures," *J. Geophys. Res.*, vol. 88(C3), pp. 1892-1908, 1983.
- [24] F. J. Wentz, L. A. Mattox, and S. Petcherych, "New algorithms for microwave measurements of ocean winds: Applications to SEASAT and the Special Sensor Microwave Imager," *J. Geophys. Res.*, vol. 91(C2), pp. 2289-2307, 1986.
- [25] F. J. Wentz, "User's manual SSM/I antenna temperature tapes," RSS Tech. Rep. 032588, 36 pp., Remote Sensing Systems, Santa Rosa, CA, Mar. 1988.
- [26] F. J. Wentz, "SBIR phase II report: West coast storm forecasting with SSM/I," RSS Tech. Rep. 033190, 378 pp., Remote Sensing Systems, Santa Rosa, CA, Mar. 1990.
- [27] F. J. Wentz, "A simplified wind-vector algorithm for satellite scatterometers," *J. Atmospheric and Oceanic Tech.*, vol. 8, no. 5, pp. 697-705, 1991.
- [28] S. T. Wu and A. K. Fung, "A noncoherent model for microwave emissions and backscattering from the sea surface," *J. Geophys. Res.*, vol. 77(30), pp. 5917-5929, 1972.



**Frank J. Wentz** was born in Jacksonville, FL, on December 28, 1946. He received the B.S. degree in physics and the M.S. degree in physics with a concentration on far-infrared astronomy, in 1969 and 1971, respectively, from the Massachusetts Institute of Technology.

From 1970 to 1974 he worked for Radiometric Technology, Inc., where he developed physical models for the microwave emission and scattering from rough ocean surfaces. In 1974 he established Remote Sensing Systems, a company specializing in satellite microwave remote sensing. From 1974 to 1981, in support of NASA's SeaSat Project, he developed geophysical retrieval algorithms for the SeaSat microwave scatterometer SASS and radiometer SMMR. The outcome of this work was an improved SMRR/SASS geophysical product. Also during this time, he conducted computer simulations that demonstrated a 3-look scatterometer could uniquely determine wind direction over the ocean. Recently, he developed a data processing system for the Special Sensor Microwave Imager (SSM/I). The SSM/I products are now being routinely distributed to the Earth science community.

Mr. Wentz has published 25 scientific papers and 60 technical reports. He is an associate editor of the *Journal of Atmospheric and Oceanic Technology* and a member of AGU. He has served on many governmental committees and working groups.